High Resolution FDMA MIMO Radar

DAVID COHEN
Rafael Advanced Defense Systems Ltd., Haifa, Israel

DEBORAH COHEN, Student Member, IEEE
Google Research, Tel Aviv, Israel

YONINA C. ELDAR, Fellow, IEEE
Weizmann Institute of Science, Rehovot, Israel

Traditional multiple-input multiple-output (MIMO) radars, which transmit orthogonal coded waveforms, suffer from range–azimuth resolution tradeoff. In this article, we adopt a frequency division multiple access (FDMA) approach that breaks this conflict. We combine narrow individual bandwidth for high azimuth resolution and large overall total bandwidth for high range resolution. We process all channels jointly to overcome the FDMA range resolution limitation to a single bandwidth, and address range–azimuth coupling using a random array configuration.

Manuscript received July 9, 2019; revised November 2, 2019; released for publication November 10, 2019. Date of publication December 9, 2019; date of current version August 7, 2020.

DOI. No. 10.1109/TAES.2019.2958193

Refereeing of this contribution was handled by Z. Davis.

The work of D. Cohen was supported by the Azrieli Foundation through Azrieli Fellowship. This work was supported in part by the European Union's Horizon 2020 research and innovation program under Grant 646804-ERC-COG-BNYQ and in part by the Israel Science Foundation under Grant 0100101.

Authors' addresses: David Cohen is with the Signal Processing Department, Rafael Advanced Defense Systems Ltd., Haifa 31021, Israel, E-mail: (davidcohenys@gmail.com); Deborah Cohen is with the Google Research, Tel Aviv 6789141, Israel, E-mail: (deborah.co88@gmail.com); Y. C. Eldar is with the Faculty of Mathematics and Computer Science, Weizmann Institute of Science, Rehovot 7610001, Israel, E-mail: (yonina.eldar@weizmann.ac.il). *(Corresponding author: David Cohen.)*

I. INTRODUCTION

Multiple-input multiple-output (MIMO) [1] radar consists of several transmit and receive antenna elements. Unlike phased-array systems, the emitted waveform from each transmitter is different, which offers more degrees of freedom [2]. Today, MIMO radars appear in many military and civilian applications including ground surveillance [3], [4], automotive radar [5], [6], interferometry [7], maritime surveillance [3], [8], through-the-wall radar imaging for urban sensing [9], and medical imaging [2], [10]. MIMO radars are generally classified into two main categories, depending on the location of the transmitting and receiving elements. The first configuration is the collocated MIMO [11] in which the elements are closely spaced relatively to the working wavelength while in the second configuration, the widely separated MIMO [12], they are distributed over a large deployment area.

MIMO radar presents significant potential for advancing state-of-the-art modern radar in terms of flexibility and performance. Collocated MIMO radar systems utilize the mutual orthogonality of the transmitted waveforms. Each of these waveforms can be extracted and associated at the receiver to a single transmitting antenna. This waveform diversity that is the heart of a MIMO radar system is the key for spatial channel separation, thus offering more degrees of freedom by processing the channels individually rather than processing the receiver input as in a classic phased-array [2]. Consequently, the performance of MIMO systems can be characterized by a virtual array corresponding to the convolution of the transmit and receive antenna locations. In principle, with the same number of antenna elements, this virtual array may be much larger and, thus, achieve higher resolution than an equivalent traditional phased array system [13]–[15].

The orthogonality requirement, however, poses new theoretical and practical challenges. Choosing proper waveforms is a critical task for the implementation of practical MIMO radar systems. In addition to the general requirements on radar waveforms such as high range resolution and low sidelobes, MIMO radar waveforms must satisfy good orthogonality properties. In practice, it is difficult to find waveform families that perfectly satisfy all these demands [16]. Comprehensive evaluation and comparison of different types of MIMO radar waveforms is presented in [17]–[19]. The main waveform families considered are time, frequency, and code division multiple access, abbreviated as TDMA, frequency division multiple access (FDMA), and CDMA, respectively. These may either be implemented in a single pulse, namely in the fast time domain, referred to as intrapulse coding, or in a pulse train, that is in the slow time domain, corresponding to interpulse coding. We focus on the former technique, which is the most popular. More details on interpulse coding may be found in [17] and [19].

An intuitive and simple way to achieve orthogonality is using TDMA, where the transmit antennas are switched from pulse to pulse, so that there is no overlap between

two transmissions [20]. Since the transmission capabilities of the antennas are not fully utilized, this approach induces significant loss of transmit power [17], resulting in signal-to-noise ratio (SNR) decrease and much shorter target detection range. More efficient schemes have been proposed, such as circulating MIMO waveforms [18]. However, this technique suffers from loss in range resolution [18], [19].

Another way to achieve orthogonality of MIMO radar waveforms is FDMA, where the signals transmitted by different antennas are modulated onto different carrier frequencies. This approach has several limitations. First, due to the linear relationship between the carrier frequency and the index of antenna element, a strong range–azimuth coupling occurs when using the classic virtual uniform linear array (ULA) configuration [16], [18], [19]. To resolve this coupling, the authors in [21]–[23] use random carrier frequencies, which creates high sidelobe levels. These may be mitigated by increasing the number of transmit antennas, which in turn increases system complexity. The second drawback of FDMA is that the range resolution is limited to a single waveform's bandwidth, rather than the overall transmit bandwidth [24], [25]. To increase range resolution, the authors of [26] and [27] use an interpulse stepped frequency waveform (SFW), utilizing the total bandwidth over the slow time [28]. However, SFW leads to range-Doppler coupling [29] and the pulse repetition frequency grows proportionally to the number of steps, increasing range ambiguities [20], [30].

In the popular CDMA approach, signals transmitted by different antennas are modulated using distinct series of orthogonal codes, so that they can be separated in the radar receiver. Although perfect orthogonality cannot be achieved in general, code families, such as Barker [31], Hadamard or Walsh [32], and Gold [33] sequences, present features close to orthogonality. CDMA requires good code design [2] and may suffer from high range sidelobes depending on cross-correlation properties of the code sequence [19].

Although the CDMA range resolution is determined by the total bandwidth as opposed to FDMA limitation to a single waveform, high resolution systems are still not easy to achieve. One of the major challenges is preservation of the narrowband assumption, which can be a limiting factor for high-resolution applications. The narrowband assumption creates a conflict between large desired bandwidth for high range resolution and large virtual aperture for high azimuth resolution. The tradeoff comes from the classic beamforming performance degradation when using wideband signals, since this operation is frequency dependent [34].

In particular, beamforming is based on combining the array elements to achieve constructive interference in a desired direction. Ideally, the signal in each element should be time delayed before summation while the exact delay of the signal is variable according to the array configuration and the desired direction. Traditional beamforming combines the elements based on a set of phase shifter values, which have been designed at the carrier frequency but applied to all frequencies within the transmission bandwidth. The phase shifter is widely adopted because it serves as a good approximation to a time delay for narrowband transmission, but most importantly, is easy to implement. However, this approximation can give rise to beam squint for a wideband signal since the phase shifter is frequency dependent as opposed to a time delay, which produces a frequency independent phase shift [35], [36]. The use of phase shifters for wideband beamforming leads to loss of gain as well as distorted range–azimuth resolution. In MIMO configurations where the virtual array is large, this may result in severe performance degradation; the beam squint can be enough to steer off the target [37].

Although considerable research has been performed on wideband processing techniques, no consensus has been reached in the literature regarding an appropriate wideband beamforming scheme. Most works consider the use and implementation of true-time delay (TTD), which is frequency independent, to address the beamforming deterioration of wideband phased arrays. TTD units are designed to provide a variable time delay over the array aperture in a constructive manner to the desired direction and may be realized in analog or in digital.

In analog TTD implementation, delay lines are located in each channel path to create a variable delay over the array. While the first analog delay lines were large and bulky, today with technology evolution modern TTD chips are available. However, analog-based methods suffer from insertion loss as well as linearity issues [36]. Furthermore, the time delay should be on the same length as the array aperture, which could be a heavy demand for large array apertures. To address the analog drawbacks, digital TTD beamforming was proposed in [38]. In digital TTD realizations, an arbitrary delay is split into integer and fractional with respect to the sampling interval. The integer delay is obtained by discarding samples while the fractional sample delay (FSD) is implemented using an FSD interpolation filter. Digital TTD beamforming requires filtering the signal received in each element to create a variable delay, which could be resource intensive in comparison with a simple phase shift. To alleviate the system overhead using digital filtering, in [39], the digital TTDs are incorporated at the subarray level while simple narrowband phase compensation is applied at the element level. Then, stretch processing is used in which the received signal is mixed with a reference signal to allow low sampling rate filtering. Moreover, the filters are implemented using the Farrow structure with reduced arithmetic complexity.

With the evolution of technology, there is increasing interest in simultaneous generation of multiple beams requiring parallel computing for their generation, which is an unacceptable demand for real-time systems with TTD beamforming. Furthermore, for MIMO radar in which all the space is uniformly lit, the hardware resources required for TTD beamforming grows rapidly since the TTDs are applied on the channels as opposed to the phased array. In [37], a smearing filter is adopted in wideband MIMO to

address the system complexity, which in turn leads to poor range resolution. Another approach for TTD realization is photonic beamforming in which the RF signal is modulated onto an optical carrier and a long fiber is integrated to delay the signal [36], [40], [41]. Although photonic beamforming has recently shown rapid development [42]–[44], it still requires radical changes in technology in order to be incorporated in systems [45].

In this article, a frequency diverse array (FDA) MIMO structure [46] is adopted in which orthogonality is achieved by using an FDMA transmission scheme. As will be explained later, FDA allows phase-shifting for wideband beamforming and, thus, provides an alternative to TTD. The term FDA radar was first proposed in 2006 [47], however, the concepts of FDA and MIMO have earlier roots. The first FDA MIMO radar, was the French radar RIAS, also known as SIAR: synthetic impulse and antenna radar and was proposed in 1984 [48]. In SIAR each transmit element sends orthogonal signals using an FDMA transmission scheme. The received signals are synthetically combined to offer range resolution according to the total bandwidth of the returned echo [49].

We present an array design and processing method that overcome FDMA drawbacks. First, to avoid range–azimuth coupling, we randomize the carrier frequencies as well as the transmit and receive locations within the virtual array aperture. The idea of randomized frequencies has been used in single antenna radars [29] that employ SFW, to resolve range-Doppler coupling. There, hopped frequency sequences, namely with randomized steps for increasing the carriers, are considered. Random arrays have been an object of research since the 1960s [50]. Recently, in [51], the authors adopt random MIMO arrays to reduce the number of elements required for targets' detection using sub-Nyquist spatial sampling principles [52]. Here, we use a random array to deal with the coupling issue while keeping the number of elements as in traditional MIMO. We empirically found that randomizing both the antenna locations and frequencies rather than the frequencies alone exhibits the better performance.

Second, we process the samples from all channels jointly exploiting frequency diversity [53], to overcome the range resolution limitation of a single bandwidth. A similar approach was used in [54] in the context of MIMO synthetic aperture radar with orthogonal frequency-division multiplexing linear frequency modulated (OFDM LFM) waveforms, where coherent processing over the channels allows to achieve range resolution corresponding to the total bandwidth. There, however, the MIMO array is composed of two ULAs, both with spacing equal to half the wavelength. While avoiding range-elevation coupling, this approach yields poor elevation resolution [15]. Furthermore, in [54], the total bandwidth is limited by the narrowband assumption [37] and, hence, perpetuates the range–azimuth resolution conflict.

One of the main contributions of this article is to show that using FDMA, the narrowband assumption may be relaxed to the individual bandwidth with appropriate signal processing. FDMA allows to achieve a large overall received bandwidth over the channels while maintaining the narrowband assumption for each channel. In particular, the beamforming in FDMA MIMO is applied over the narrowband channels rather than broadband channels like in CDMA. Therefore, FDMA MIMO enables phase shifters design with respect to the carrier of each narrowband channel while cooperative processing of the channels allows range resolution of broadband signals. This approach provides an alternative to the complex TTD beamforming by simple phase shifting of the narrowband channels with enhanced range–azimuth resolution capabilities. The range–azimuth resolution conflict may, thus, be solved by enabling large aperture for high azimuth resolution along with large total bandwidth for high range resolution. The narrowband assumption holds by requiring small individual bandwidth, breaking the traditional range–azimuth tradeoff.

In order to achieve range resolution corresponding to the overall bandwidth, we develop a recovery method that coherently processes all channels. This overcomes the FDMA range resolution limitation to a single bandwidth. In addition, to exploit the targets sparsity, we developed an iterative dictionary based approach. Our frequency domain processing is easily extended to sub-Nyquist recovery with low-rate sampling and reduced number of elements [55], [56]. However, our principles are valid also for noniterative approaches and could be shown in the time domain using classic matched filter components and phase shifters over the channels.

The main contributions of our approach are as follows.

1) **Enhanced range–azimuth resolution capabilities:** The FDA-MIMO framework provides an alternative for TTD beamforming by simple phase shifters with respect to each channel. Our approach simultaneously allows large aperture for high azimuth resolution along with large total bandwidth for high range resolution.
2) **Range angle decoupling:** We propose a random array configuration with random carrier allocation. Placing the antenna elements at random locations adds more degrees of freedom for better control of the sidelobes level.
3) **Iterative joint processing:** We coherently process all channels, thus enabling range resolution according to the total bandwidth with azimuth resolution governed by the virtual array aperture. The iterative approach enables sidelobe suppression and provides robustness to high dynamic range environments.

This article is organized as follows. In Section II, we review classic MIMO radar and processing. Our FDMA model is introduced in Section III, where range–azimuth coupling and range–azimuth beamforming are discussed. Section IV presents the proposed range–azimuth-Doppler recovery. Numerical experiments are presented in Section V, demonstrating the improved performance of our FDMA approach over classical CDMA. Finally, Section VI concludes this article.

II. CLASSIC MIMO RADAR

This section provides an overview of the classic MIMO radar architecture, in terms of array construction and waveforms, as well as traditional MIMO signal processing.

A. MIMO Architecture

In contrast to classic phased array, MIMO radar systems transmit orthogonal waveforms in each of the transmitting antennas. Therefore, the echo signals collected by the receiver can be reassigned to the source by performing correlation using a set of matched filters adapted to each of the transmitted waveforms. For example, if a MIMO radar has five transmit antennas and three receive antennas, then 15 signals can be extracted from the receiver due to the orthogonality property of the transmitted waveforms. Each of the extracted signals contains the information of an individual spatial channel from one of the transmitting antennas to one of the receiving antennas. This waveform diversity in MIMO radar results in more degrees of freedom by enabling processing the orthogonal channels in each receiver separately as opposed to traditional phased array.

The channel's response to a specific direction can be characterized by a differential phase induced by the transmitter and receiver array geometry, leading to the virtual array concept. A virtual array is an equivalent array whose response is the same as the channels response of a MIMO array. Specifically, the antennas locations of the virtual array correspond to the convolution of the transmit and receive antenna locations. The performance of MIMO radar is characterized by a virtual array with a larger number of elements and enlarged aperture than the physical aperture of the MIMO array.

The classic approach to collocated MIMO is based on the virtual ULA structure [57], where T transmitters, spaced by $R\frac{\lambda}{2}$ and R receivers, spaced by $\frac{\lambda}{2}$ (or vice versa), create two ULAs. Here, λ is the wavelength. The resulting TR channels are coherently processed to form a virtual array in which each element corresponds to a single channel in the MIMO structure. The resulting virtual array is equivalent to a phased array with TR $\frac{\lambda}{2}$-spaced receivers and aperture $Z = \frac{TR}{2}$ normalized to the wavelength.

Denote by $\{\xi_m\}_{m=0}^{T-1}$ and $\{\zeta_q\}_{q=0}^{R-1}$, the transmitters and receivers' normalized locations, respectively. For the traditional virtual ULA structure, $\zeta_q = \frac{q}{2}$ and $\xi_m = R\frac{m}{2}$. This classic array structure and the resulting virtual array are illustrated in Fig. 1 for $R = 4$ and $T = 4$ where each color represents the channels induced by a single transmit element. In our work, we consider a random array configuration [51], where the antennas' locations are chosen uniformly at random within the aperture of the virtual array described earlier, that is $\{\xi_m\}_{m=0}^{M-1} \sim \mathcal{U}[0, Z]$ and $\{\zeta_q\}_{q=0}^{Q-1} \sim \mathcal{U}[0, Z]$, respectively. The corresponding virtual array has the same or a greater aperture than a traditional virtual array with the same number of elements, depending on the locations of the antennas at the far edges. The resulting azimuth resolution is thus at least as good as that of the traditional virtual ULA structure.

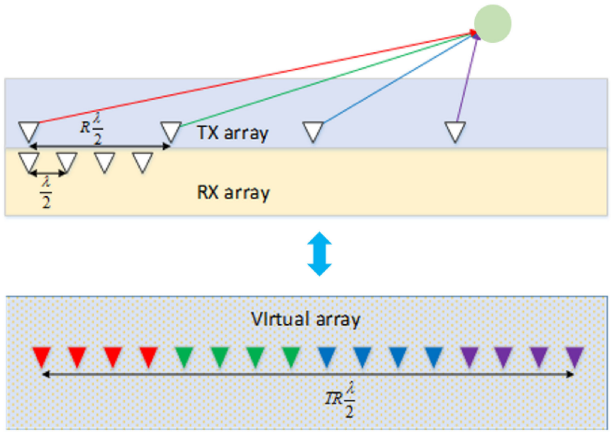

Fig. 1. Illustration of MIMO arrays and the corresponding receiver virtual array.

Each transmitting antenna emits P pulses, such that mth transmitted signal can be expressed as

$$s_m(t) = \sum_{p=0}^{P-1} s_m^p(t), \quad 0 \le t \le P\tau, \tag{1}$$

where

$$s_m^p(t) = h_m\left(t - p\tau\right)e^{j2\pi f_c t}. \tag{2}$$

Here, $h_m(t)$, $0 \le m \le T-1$, are orthogonal waveforms with bandwidth B_h and carrier frequency f_c. The pulses are transmitted within the coherent processing interval (CPI) that is equal to $P\tau$, where τ denotes the pulse repetition interval (PRI). The pulse time width is denoted by T_w, with $0 < T_w < \tau$.

The orthogonality property in MIMO radar places additional requirements on the transmitted waveforms. This property is added to the classic demands from the radar ambiguity function such as low sidelobes and resolution [28]. Moreover, to avoid cross talk between the T signals and to ensure TR uncorrelated channels, the orthogonality condition should be also invariant to time shifts, that is $\int_{-\infty}^{\infty} s_i(t)s_j^*(t-\tau_0)dt = \delta(i-j)$, for $i, j \in [0, T-1]$ and for all τ_0. This implies that the orthogonal transmitted waveforms cannot overlap in frequency (or time) [37], leading to the FDMA (or TDMA) approach. Alternatively, time invariant orthogonality may be approximately attained using CDMA.

Both FDMA and CDMA can be expressed by the general model [18]:

$$h_m(t) = \sum_{u=1}^{N_c} w_{mu}e^{j2\pi f_{mu}t}v(t - u\delta_t), \tag{3}$$

where each pulse consists of N_c time slots with duration δ_t. Here, $v(t)$ denotes the fundamental waveform, w_{mu} represents the code, and f_{mu} represents the frequency for the mth transmission and uth time slot. The different waveform families follow the general expression (3) and can be analyzed accordingly. In particular, in CDMA, orthogonality is attained by the code $\{w_{mu}\}_{u=1}^{N_c}$ and $f_{mu} = 0$ for all

$1 \le u \le N_c$. FDMA presents no coding, i.e., $N_c = 1$, $w_{mu} = 1$, and $\delta_t = 0$. The orthogonality is then achieved by center frequencies $f_{mu} = f_m$ that are selected in $[-\frac{TB_h}{2}, \frac{TB_h}{2}]$ so that the intervals $[f_m - \frac{B_h}{2}, f_m + \frac{B_h}{2}]$ do not overlap. For FDMA, transforming (3) from the time domain into the frequency domain, $\{h_m(t)\}_{m=0}^{T-1}$ can be considered as frequency-shifted versions of a low-pass pulse $v(t) = h_0(t)$, such that

$$H_m(\omega) = H_0\left(\omega - 2\pi f_m\right). \tag{4}$$

Here, $H_0(\omega)$ denotes the Fourier transform of $h_0(t)$ with bandwidth B_h. For simplicity, a unified notation is adopted for the total bandwidth, $B_{\text{tot}} = TB_h$ for FDMA and $B_{\text{tot}} = B_h$ for CDMA.

B. Received Signal

Consider L point-targets within the area covered by the radar. Each target illuminated by the radar is with initial range R_l to the array origin and moving with radial velocity v_l along the line of sight with azimuth angle θ_l relative to the array. Our objective is to recover the targets' delay $\tau_l = \frac{2R_l}{c}$, azimuth sine $\vartheta_l = \sin(\theta_l)$, and Doppler shift $f_l^D = \frac{2v_l}{\lambda}$ from the received signals. Throughout this article, we will use interchangeably the terms range and delay, as well as azimuth angle and sine, and velocity and Doppler frequency.

The transmitted pulses are reflected from the targets back and acquired by the receive antennas. To simplify the received signal expression, the following assumptions are adopted on the targets' location and motion with respect to the array structure as well as transmitted signal properties.

A1) Collocated array - the target scattering complex coefficient α_l and angle θ_l are constant over the array (see [58] for more details).

A2) Swerling-0 model - the target radar cross section (RCS) has no fluctuation [59], allowing for constant α_l.

A3) Stop-and-hop assumption - targets stop during transmission and reception of a single pulse [60]. Specifically, the phase induced by the relative target motion is negligible

$$\frac{2v_l^2 P\tau}{\lambda c} \ll 1, \tag{5}$$

and the Doppler phase during the pulse width T_w can be ignored

$$f_l^D T_w \ll 1. \tag{6}$$

A4) Free-range migration - the target motion within the CPI is less than the range resolution [61], allowing for constant τ_l

$$\frac{2v_l P\tau}{c} \ll \frac{1}{B_{\text{tot}}}. \tag{7}$$

A5) Free-Doppler spread - the Doppler change within the CPI is less than the Doppler resolution [61], allowing for constant Doppler shift f_l^D

$$\dot{f_l^D} P\tau \ll \frac{1}{P\tau}. \tag{8}$$

A6) Narrowband waveform - small aperture allows τ_l to be constant over the channels

$$\frac{2Z\lambda}{c} \ll \frac{1}{B_{\text{tot}}}. \tag{9}$$

Under Assumptions A1–A3 and A5, the received signal $x_q(t)$ at the qth antenna is a sum of time-delayed, scaled replica of the transmitted signals

$$x_q(t) = \sum_{p=0}^{P-1}\sum_{m=0}^{T-1}\sum_{l=1}^{L} \alpha_l s_m^p\left(t - \frac{R_{l,mq}(p\tau)}{c}\right), \tag{10}$$

where $R_{l,mq}(t) = 2R_l + 2v_l t - (R_{lm} + R_{lq})$, with $R_{lm} = \lambda\xi_m\vartheta_l$ and $R_{lq} = \lambda\zeta_q\vartheta_l$ accounting for the array geometry. The received signal can be simplified using Assumptions A4 and A6, as we now show.

We start with the envelope $h_m(t)$, and consider the pth PRI and the lth target. From A4, we neglect the term $\frac{2v_l p\tau}{c}$ and obtain

$$h_m\left(t - \frac{R_{l,mq}(p\tau)}{c}\right) = h_m(t - p\tau - \tau_{l,mq}). \tag{11}$$

Here, $\tau_{l,mq} = \tau_l - \eta_{mq}\vartheta_l$ where $\tau_l = \frac{2R_l}{c}$ is the target delay, and $\eta_{mq} = (\xi_m + \zeta_q)\frac{\lambda}{c}$ follows from the respective locations between transmitter and receiver. We then add the modulation term of $s_m(t)$ and after down-conversion to baseband and ignoring constant phases, the remaining term is given by

$$h_m(t - p\tau - \tau_{l,mq}) e^{j2\pi f_c \eta_{mq}\vartheta_l} e^{-j2\pi f_l^D p\tau}. \tag{12}$$

Finally, from A6, the delay term $\eta_{mq}\vartheta_l$, which stems from the array geometry, is neglected in the envelope which becomes

$$h_m(t - p\tau - \tau_l). \tag{13}$$

Substituting (13) into (12), the received signal at the qth antenna after demodulation to baseband is given by

$$x_q(t) = \sum_{p=0}^{P-1}\sum_{m=0}^{T-1}\sum_{l=1}^{L} \alpha_l h_m\left(t - p\tau - \tau_l\right) e^{j2\pi f_c \eta_{mq}\vartheta_l} e^{-j2\pi f_l^D p\tau}. \tag{14}$$

The narrowband Assumption A6 leads to a tradeoff between azimuth and range resolution, by requiring either small aperture Z or small total bandwidth B_{tot}, respectively. In CDMA, $B_{\text{tot}} = B_h$ so that A6 limits the total bandwidth of the waveforms $h_m(t)$ [37]. This is illustrated in Fig. 2 that shows the performance of CDMA waveforms using the classical processing detailed as follows. We use bandlimited Gaussian pulses that are equivalent to CDMA, where each transmitter radiates $P = 1$ pulse, and consider range–azimuth recovery in the absence of noise. We assume $L = 5$ targets whose locations are generated uniformly at random, and adopt a hit-or-miss criterion according to the Rayleigh resolution as our performance metric. A "hit" is defined as a range–azimuth estimate that is identical to the true target position up to one Nyquist bin (grid point) defined as $1/B_{\text{tot}}$ and $2/TR$ for the range and azimuth, respectively.

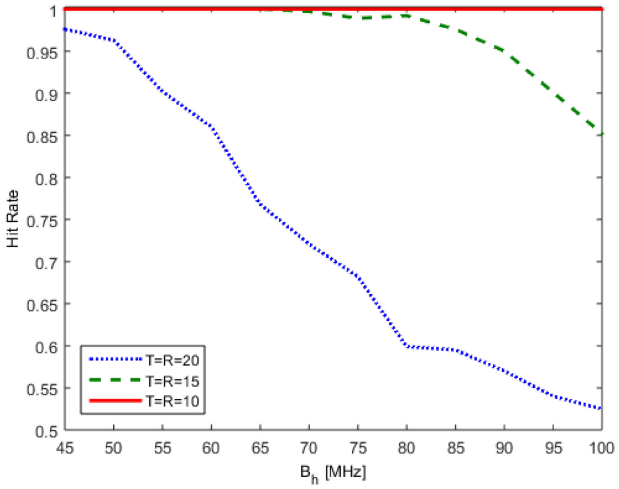

Fig. 2. Hit rate of MIMO radar with classical processing of CDMA waveforms with respect to total bandwidth $B_{\text{tot}} = B_h$ and aperture $Z = TR/2$.

Each experiment is repeated over 200 realizations. It can be seen that the recovery performance decreases with either increased bandwidth or aperture since in both cases A6 does not hold. In the subsequent section, We show that in the FDMA processing framework, the assumption can be relaxed so that the aperture is required to be smaller than the reciprocal of B_h rather than $B_{\text{tot}} = TB_h$ as in (9).

C. Range–Azimuth-Doppler Recovery

The traditional collocated MIMO radar processing scheme includes the following steps.

1) **Sampling:** The received signal $x_q(t)$ is sampled at its Nyquist rate B_{tot} at each receiver element.
2) **Matched filter:** The sampled signal is correlated with a sampled version of $h_m(t)$, for $0 \le m \le T-1$. The time resolution attained in this step is $1/B_h$. In FDMA, this step leads to a limitation on the range resolution to a single channel bandwidth rather than the total bandwidth.
3) **Beamforming:** The matched filter output is correlated over the channels with steering vectors corresponding to each azimuth grid point. The spatial resolution attained in this step is $2/TR$. In FDMA, this stage leads to range–azimuth coupling, as illustrated in Section III-D.
4) **Doppler processing:** Spectral analysis is performed over the pulses of the resulting vectors for detection of Doppler frequencies. The Doppler resolution attained in this step is $1/P\tau$.
5) **Detection:** A detection process is applied on the resulting range–azimuth-Doppler map. The detection can follow a threshold approach [62] to preserve false alarm requirements or select the L strongest point of the map, if the number of targets L is known.

CDMA is a popular MIMO approach even though it suffers from two main drawbacks. First, the narrowband assumption yields a tradeoff between azimuth and range resolution. Second, achieving orthogonality through code

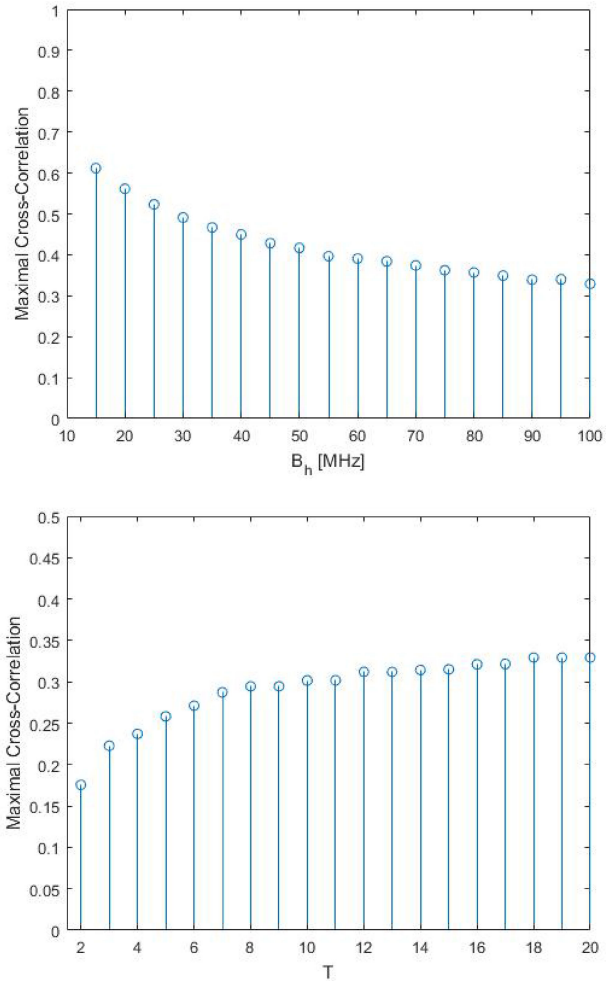

Fig. 3. Maximal cross correlation of CDMA waveforms using $T_w = 0.44$ μs with respect to signal bandwidth B_h with $T = 20$ transmitters (top) and number of transmitters T with bandwidth $B_h = 100$ MHz (bottom).

design has proven to be a challenging task [2]. To illustrate this, we consider a set of orthogonal bandlimited Gaussian waveforms, generated using a random search for minimizing the cross correlation between pairs of waveforms. That is, the set of waveforms is constructed so as to minimize the maximal cross correlation between waveforms, through a nonexhaustive search. Fig. 3 shows the maximal cross correlations between any pair of signals within the set. It can be seen that, when either the bandwidth B_h is reduced or the number of transmit antennas increases, the maximal cross correlation of the CDMA waveforms increases.

Meanwhile, classic FDMA has been almost neglected owing to its two main drawbacks. First, a strong range–azimuth coupling results from frequency diversity along the channels [16], [18], [19], as we illustrate in Section III-D. The second drawback of FDMA is that the range resolution is dictated by a single waveform's bandwidth, namely B_h, rather than the overall transmit bandwidth $B_{\text{tot}} = TB_h$ [24], [25]. In the following section, we adopt the FDMA approach, in order to exploit the narrowband property of each individual channel to achieve both high range and

azimuth resolution. To address the coupling issue, the antenna elements are uniformly distributed over the aperture, while keeping the random carrier frequencies on a grid with spacing B_h. Next, by joint processing of the channels, we attain a range resolution of $1/B_{\text{tot}} = 1/TB_h$ rather than $1/B_h$. This way, we utilize the overall received bandwidth for range resolution enhancement, while preserving the narrowband assumption for each channel, paving the way to high azimuth resolution. In addition, no code design is required, which may be a challenging task [2], as shown in Fig. 3.

III. FDMA SYSTEM

We now describe our MIMO system based on joint channel processing of FDMA waveforms. Our FDMA processing differs from the classic CDMA approach introduced in Section II in several aspects. First, the single channel processing, which is equivalent to matched filtering in step (2), is limited to $1/B_h = T/B_{\text{tot}}$ whereas in CDMA, we achieve resolution of $1/B_{\text{tot}}$. In addition, in FDMA, the range depends on the channels while in CDMA, it is decoupled from the channels domain. Therefore, our processing involves range–azimuth beamforming while the classic approach for CDMA uses beamforming on the azimuth domain only as in step (3). The range dependency on the channels in FDMA is exploited to enhance the poor range resolution of the single channel $1/B_h$ to $1/TB_h = 1/B_{\text{tot}}$, as explained in the remainder of this section. Finally, combining the use of FDMA waveforms with our proposed processing reconciles the narrowband assumption with large total bandwidth for range resolution, enhancing range–azimuth resolution capabilities.

A. Received Signal Model

Our FDMA framework followed by appropriate processing, described in Section IV, allows to alleviate the rigid restrictions induced by A6. In FDMA, the strict neglect of the delay term can be substantially reduced in the transition from (12) to (13). Specifically, we confine the $\eta_{mq}\vartheta_l$ term removal to the envelope $h_0(t)$ rather than $h_m(t)$. Then, (13) becomes

$$h_m(t - p\tau - \tau_l)e^{j2\pi f_m \eta_{mq}\vartheta_l}. \tag{15}$$

Here, the delays governed by the array geometry are maintained over the channels, relaxing A6 to $\frac{2Z\lambda}{c} \ll \frac{1}{B_h}$. We recall that under the CDMA framework, A6 leads to a compromise between azimuth and range resolution, by limiting the array aperture or the total bandwidth. Here, using the FDMA framework and the approximation (15), the total bandwidth $B_{\text{tot}} = TB_h$ is not limited and we need only the single bandwidth B_h to be narrow. As we show in the following, the resolution is governed by the total bandwidth, thus eliminating the tradeoff between range and azimuth resolution.

The received signal at the qth antenna after demodulation to baseband is in turn given by

$$x_q(t) = \sum_{p=0}^{P-1}\sum_{m=0}^{T-1}\sum_{l=1}^{L} \alpha_l h_m\left(t - p\tau - \tau_l\right) e^{j2\pi\beta_{mq}\vartheta_l} e^{-j2\pi f_l^D p\tau}, \tag{16}$$

where $\beta_{mq} = (\zeta_q + \xi_m)(f_m\frac{\lambda}{c} + 1)$. In comparison with (14), neglecting the delay term only in the narrowband envelope $h_0(t)$, (16) results in the extra term $e^{j2\pi(\zeta_q+\xi_m)\vartheta_l f_m\lambda/c}$. This corrects the time of arrival differences between channels, so that the narrowband assumption is required only on $h_0(t)$ with bandwidth B_h and not on the entire bandwidth B_{tot}. Intuitively, the waveforms are aligned to eliminate the arrival differences resulting from the array geometry with respect to f_m, thus enabling to detect the azimuth with respect to the central carrier f_c. This assumption does not require additional steps on the processing and allows keeping simple phase shifting beamforming over the channels. The phases are simply updated to account for the carrier frequency of each narrowband channel, thus providing an alternative to the complicated TTD beamforming.

It will be convenient to express $x_q(t)$ as a sum of single PRIs

$$x_q(t) = \sum_{p=0}^{P-1} x_q^p(t), \tag{17}$$

where

$$x_q^p(t) = \sum_{m=0}^{T-1}\sum_{l=1}^{L} \alpha_l h_m(t - p\tau - \tau_l)e^{j2\pi\beta_{mq}\vartheta_l} e^{-j2\pi f_l^D p\tau}. \tag{18}$$

Our goal is to estimate the targets range, azimuth, and velocity, i.e., to estimate τ_l, ϑ_l, and f_l^D from $x_q(t)$.

B. Frequency Domain Analysis

We begin by deriving an expression for the Fourier coefficients of the received signal, and show how the unknown parameters, namely τ_l, ϑ_l, and f_l^D are embodied in these coefficients. We next turn to range–azimuth beamforming and its underlying resolution capabilities and discuss the range–azimuth coupling. Finally, we present our proposed recovery algorithm, which is based on FDMA waveforms. To introduce our processing, we start with the special case of $P = 1$, namely a single pulse is transmitted by each transmit antenna. We show how the range–azimuth map can be recovered from the Fourier coefficients in time and space. Subsequently, we treat the general case where a train of $P > 1$ pulses is transmitted by each antenna, and present a joint range–azimuth-Doppler recovery algorithm from the Fourier coefficients.

The pth PRI of the received signal at the qth antenna, namely $x_q^p(t)$, is limited to $t \in [p\tau, (p+1)\tau]$ and, thus, can be represented by its Fourier series

$$x_q^p(t) = \sum_{k\in\mathbb{Z}} c_q^p[k]\, e^{j2\pi kt/\tau}, \quad t \in \left[p\tau, (p+1)\tau\right], \tag{19}$$

where for $-\frac{NT}{2} \le k \le \frac{NT}{2} - 1$, with $N = \tau B_h$

$$c_q^p[k] = \frac{1}{\tau} \sum_{m=0}^{T-1} \sum_{l=1}^{L} \alpha_l e^{j2\pi\beta_{mq}\vartheta_l} e^{-j\frac{2\pi}{\tau}k\tau_l} e^{-j2\pi f_l^D p\tau} H_m\left(\frac{2\pi}{\tau}k\right). \tag{20}$$

Once the Fourier coefficients $c_q^p[k]$ are computed, we separate them into channels for each transmitter, by exploiting the fact that they do not overlap in frequency. Applying a matched filter, we have

$$\begin{aligned}\tilde{c}_{q,m}^p[k] &= c_q^p[k] H_m^*\left(\frac{2\pi}{\tau}k\right) \\ &= \frac{1}{\tau}\left|H_m\left(\frac{2\pi}{\tau}k\right)\right|^2 \sum_{l=1}^{L} \alpha_l e^{j2\pi\beta_{mq}\vartheta_l} e^{-j\frac{2\pi}{\tau}k\tau_l} e^{-j2\pi f_l^D p\tau}.\end{aligned} \tag{21}$$

Let $y_{m,q}^p[k] = \frac{\tau}{|H_0(\frac{2\pi}{\tau}k)|^2}\tilde{c}_{q,m}^p[k + f_m\tau]$ be the normalized and aligned Fourier coefficients of the channel between the mth transmitter and qth receiver. Then,

$$y_{m,q}^p[k] = \sum_{l=1}^{L} \alpha_l e^{j2\pi\beta_{mq}\vartheta_l} e^{-j\frac{2\pi}{\tau}k\tau_l} e^{-j2\pi f_m\tau_l} e^{-j2\pi f_l^D p\tau}, \tag{22}$$

for $-\frac{N}{2} \le k \le \frac{N}{2} - 1$. Our goal then is to recover the targets' parameters τ_l, θ_l ϑ_l, and f_l^D from $y_{m,q}^p[k]$.

C. Range–Azimuth Beamforming

Let us now pause to discuss the range and azimuth resolution capabilities of the described model and processing as well as the coupling issue between the two parameters. Since the Doppler frequency is decoupled from the range–azimuth domain, we assume that $P = 1$ for the sake of clarity. Then, (22) can be simplified to

$$y_{m,q}[k] = \sum_{l=1}^{L} \alpha_l e^{j2\pi\beta_{mq}\vartheta_l} e^{-j\frac{2\pi}{\tau}k\tau_l} e^{-j2\pi f_m\tau_l}, \tag{23}$$

for $-\frac{N}{2} \le k \le \frac{N}{2} - 1$. The azimuth is embodied in the first term and its resolution is related to the virtual array geometry governed by β_{mq} as discussed in [15]. The delay is embodied in the second and third terms, which allows both high range resolution and large unambiguous range. The second term leads to a poor range resolution of $1/B_h$ corresponding to a single channel, while the resolution induced by the third term, which measures the effect of the delay on the transmit carrier, is dictated by the total bandwidth, namely $1/TB_h$. On the other hand, since f_m is a multiple of B_h in our configuration, the last term is periodic in τ_l with a limited period of $1/B_h$, whereas the second term is periodic in τ_l with period τ so that the corresponding unambiguous range is $c\tau/2$. Therefore, by jointly processing both terms, we overcome the resolution and ambiguous range limitations, and thus, achieve a range resolution of $1/TB_h$ with unambiguous range of τ, as summarized in Table I.

Both the first and third terms, which contain the azimuth and delay, respectively, depend on the channels indexed by m, q and, thus, need to be resolved simultaneously. This processing step is referred to as range–azimuth beamforming and will be discussed in the following section. The joint processing, which combines single-channel processing and range–azimuth beamforming, is illustrated in Fig. 4. The poor range resolution that would be obtained by processing each channel separately can be seen in Fig. 4(a). Range–azimuth beamforming, illustrated in Fig. 4(b), achieves a higher resolution of $1/TB_h$, corresponding to the total bandwidth. However, the resulting range ambiguity can be clearly observed. Combining the single channel processing with range–azimuth beamforming yields joint range–azimuth recovery [see Fig. 4(c)]. Note that the processing is not divided into these two steps, which are provided for illustration purposes only.

TABLE I
Range Resolution and Ambiguity

Term	Range Resolution	Unambiguous Range
$e^{-j\frac{2\pi}{\tau}k\tau_l}$	$1/B_h$	τ
$e^{-j2\pi f_m\tau_l}$	$1/TB_h$	$1/B_h$
Joint Processing	$1/TB_h$	τ

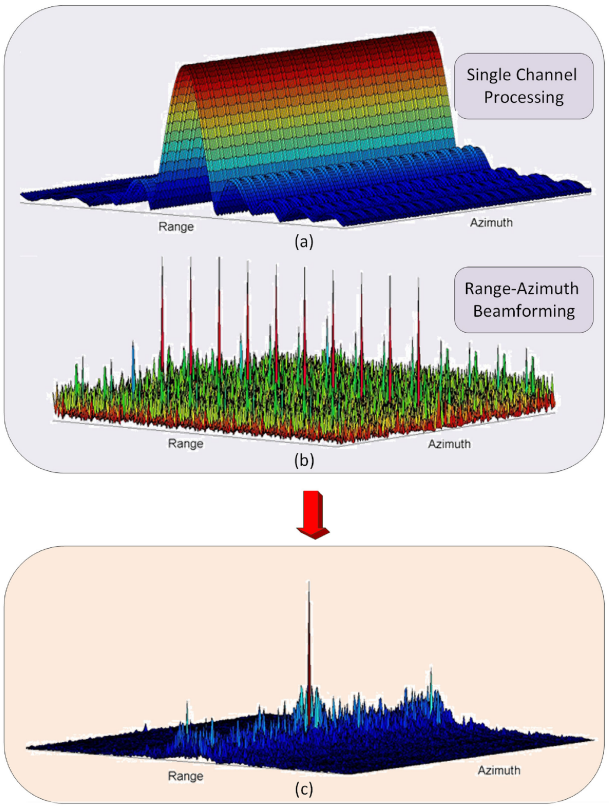

Fig. 4. Illustration of the resolution obtained by processing a single channel and by joint processing of all channels, using range–azimuth beamforming.

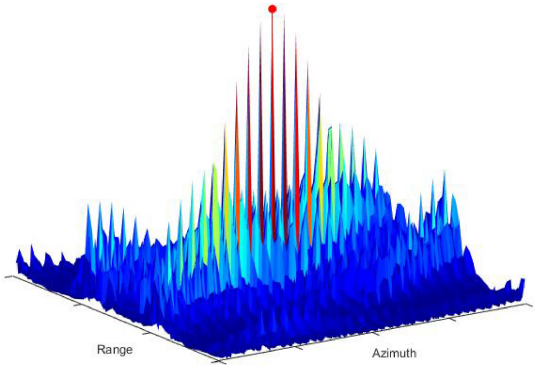

Fig. 5. Range–azimuth map in noiseless settings for antennas located on the conventional ULA and carrier frequencies selected on a grid, with $L = 1$ target. The highest peak with the red circle corresponds to the true target. The other peaks results from the range–azimuth coupling [55].

D. Range–Azimuth Coupling

As explained earlier, range–azimuth beamforming over the channels involves the estimation of both parameters from one dimension, the channel dimension. Therefore, it requires a one-to-one correspondence between the phases over the channels to range–azimuth pairs in order to prevent coupling. This ensures that each phase over the channels, expressed by the first and third terms of (23), corresponds to a unique azimuth-range pair. We next illustrate the range–azimuth coupling which occurs, in particular, in the case where the antennas are located according to the conventional virtual ULA structure shown in Fig. 1, and the carrier frequencies are selected on a grid such that $f_m = (m - \frac{T-1}{2})B_h$.

In the single pulse case, where $P = 1$, we can rewrite (23) with respect to the channel $\gamma = mR + q$ as

$$y_\gamma[k] = \sum_{l=1}^{L} a_l e^{j2\pi\beta_\gamma\vartheta_l} e^{-j2\pi f_\gamma\tau_l} e^{-j\frac{2\pi}{\tau}k\tau_l}, \tag{24}$$

where $\beta_\gamma = \gamma/2$, $f_\gamma = (\gamma \bmod T)B_h$, and a_l is equal to α_l up to constant phases. Assume that τ_l and ϑ_l lie on the Nyquist grid such that

$$\begin{aligned}\tau_l &= \frac{\tau}{TN}s_l,\\ \vartheta_l &= -1 + \frac{2}{TR}r_l,\end{aligned} \tag{25}$$

where s_l and r_l are integers satisfying $0 \le s_l \le TN - 1$ and $0 \le r_l \le TR - 1$, respectively. Then, (24) becomes

$$y_\gamma[k] = \sum_{l=1}^{L} a_l e^{j2\pi\frac{\gamma}{TR}(r_l - s_l R)} e^{-j\frac{2\pi}{TN}ks_l}, \tag{26}$$

for $-\frac{N}{2} \le k \le \frac{N}{2} - 1$. We observe that the first term is ambiguous with respect to the range and azimuth, and therefore, the range–azimuth beamforming is ambiguous. In noiseless settings, we can recover the range and azimuth with no ambiguity from the second term (single channel). This is illustrated in Fig. 5, where the highest peak in the range–azimuth map corresponds to the true target. However, this configuration may lead to ambiguity between both parameters in the presence of noise, due to other high peaks. We, thus, choose to adopt a random array, as discussed in Section V.

IV. RANGE–AZIMUTH-DOPPLER RECOVERY

We now describe our recovery approach from the Fourier coefficients of the FDMA received waveforms (16). We first consider the case where $P = 1$ and derive range–azimuth recovery from the coefficients (23). We next turn to range–azimuth-Doppler recovery from (22).

A. Range–Azimuth Recovery

In practice, as in traditional MIMO, suppose we now limit ourselves to the Nyquist grid with respect to the total bandwidth TB_h so that τ_l and ϑ_l lie on the grid defined in (25). Let $\mathbf{Y}^m$ be the $N \times R$ matrix with qth column given by $y_{m,q}[k - N/2]$, defined in (23), for $0 \le k \le N - 1$. We can write $\mathbf{Y}^m$ as

$$\mathbf{Y}^m = \mathbf{A}^m\mathbf{X}\left(\mathbf{B}^m\right)^T. \tag{27}$$

Here, $\mathbf{A}^m$ denotes the $N \times TN$ matrix whose (k, n)th element is $e^{-j\frac{2\pi}{TN}(k-\frac{N}{2})n}e^{-j2\pi\frac{f_m}{B_h}\frac{n}{T}}$ and $\mathbf{B}^m$ is the $R \times TR$ matrix with (q, p)th element $e^{j2\pi\beta_{mq}(-1+\frac{2}{TR}p)}$. The matrix $\mathbf{X}$ is a $TN \times TR$ sparse matrix that contains the values α_l at the L indices (s_l, r_l).

Our goal is to recover $\mathbf{X}$ from the measurement matrices $\mathbf{Y}^m$, $0 \le m \le M - 1$. The time and spatial resolution induced by $\mathbf{X}$ are $\frac{\tau}{TN} = \frac{1}{TB_h}$, and $\frac{2}{TR}$, respectively, as in classic CDMA processing.

Define

$$\mathbf{A} = [\mathbf{A}^{0^T}\ \mathbf{A}^{1^T}\ \cdots\ \mathbf{A}^{(T-1)^T}]^T, \tag{28}$$

and

$$\mathbf{B} = [\mathbf{B}^{0^T}\ \mathbf{B}^{1^T}\ \cdots\ \mathbf{B}^{(T-1)^T}]^T. \tag{29}$$

The matrices $\mathbf{A}$ and $\mathbf{B}$ are generally described as dictionaries, whose columns correspond to the range and azimuth grid points, respectively. To better understand the structure of $\mathbf{A}$ and $\mathbf{B}$, consider the case when the carriers f_m lie on the grid $f_m = (m - \frac{T-1}{2})B_h$ and the array constructions is according to virtual array configuration as illustrated in Fig. 1. In this case, under the Assumption A6 the resulting $\mathbf{A}$ and $\mathbf{B}$ matrices are Fourier matrices up to row or column permutation. However, this configuration leads to range–azimuth coupling as discussed in Section III-D. In Section V, we use a random array and random carrier allocation to avoid range–azimuth coupling.

One approach to solving (27) is based on CS [52], [63] techniques that exploits the sparsity of the target scene. One of CS recovery advantages is that it allows to reduce the number of required samples, pulses, and channels while preserving the underlying resolution [55]. In particular, we adopt an iterative reconstruction approach that is beneficial when dealing with high dynamic range with both weak and strong targets, especially since the sidelobes are slightly raised due to the random array configuration. Our recovery

Algorithm 1: Simultaneous 2D Recovery Based OMP.

Input: Observation matrices $\mathbf{Y}^m$, measurement matrices $\mathbf{A}^m$, $\mathbf{B}^m$, for all $0 \le m \le T-1$

Output: Index set Λ containing the locations of the non zero indices of $\mathbf{X}$, estimate for sparse matrix $\hat{\mathbf{X}}$

1: Initialization: residual $\mathbf{R}_0^m = \mathbf{Y}^m$, index set $\Lambda_0 = \emptyset$, $t = 1$

2: Project residual onto measurement matrices:

$$\mathbf{\Psi} = \mathbf{A}^H \mathbf{R} \bar{\mathbf{B}}$$

where $\mathbf{A}$ and $\mathbf{B}$ are defined in (28) and (29), respectively, and $\mathbf{R} = \text{diag}([\mathbf{R}_{t-1}^0 \cdots \mathbf{R}_{t-1}^{T-1}])$ is block diagonal

3: Find the two indices $\lambda_t = [\lambda_t(1) \quad \lambda_t(2)]$ such that

$$[\lambda_t(1) \quad \lambda_t(2)] = \arg\max_{i,j} \left|\mathbf{\Psi}_{i,j}\right|$$

4: Augment index set $\Lambda_t = \Lambda_t \bigcup \{\lambda_t\}$

5: Find the new signal estimate

$$\hat{\alpha} = [\hat{\alpha}_1 \ \ldots \ \hat{\alpha}_t]^T = (\mathbf{D}_t^T \mathbf{D}_t)^{-1} \mathbf{D}_t^T \text{vec}(\mathbf{Y})$$

6: Compute new residual

$$\mathbf{R}_t^m = \mathbf{R}_0^m - \sum_{l=1}^{t} \alpha_l \mathbf{a}^m_{\Lambda_t(l,1)} \left(\mathbf{b}^m_{\Lambda_t(l,2)}\right)^T$$

7: If $t < L$, increment t and return to step 2, otherwise stop

8: Estimated support set $\hat{\Lambda} = \Lambda_L$

9: Estimated matrix $\hat{\mathbf{X}}$: $(\Lambda_L(l,1), \Lambda_L(l,2))$-th component of $\hat{\mathbf{X}}$ is given by $\hat{\alpha}_l$ for $l = 1, \ldots, L$ while the rest of the elements are zero

algorithm is based on orthogonal matching pursuit (OMP) [52], [63]. Similar subtraction techniques are used in many iterative algorithms such as the CLEAN process [64].

To recover the sparse matrix $\mathbf{X}$ from the set of equations (27), for all $0 \le m \le M-1$, where the targets' range and azimuth lie on the Nyquist grid, we consider the following optimization problem

$$\min ||\mathbf{X}||_0 \text{ s.t. } \mathbf{A}^m \mathbf{X} \left(\mathbf{B}^m\right)^T = \mathbf{Y}^m, \quad 0 \le m \le T-1. \tag{30}$$

It has been shown in [55] that the minimal number of channels required for perfect recovery of $\mathbf{X}$ in (30) with L targets in noiseless settings is $TR \ge 2L$ with a minimal number of $TN \ge 2L$ samples per receiver. To solve (30), we extend the matrix OMP from [65] to simultaneously solve a system of CS matrix equations, as shown in Algorithm 1. In the algorithm description, $\text{vec}(\mathbf{Y}) \triangleq [\text{vec}(\mathbf{Y}^0)^T \cdots \text{vec}(\mathbf{Y}^{T-1})^T]^T$, $\mathbf{d}_t(l) = [(\mathbf{d}_t^0(l))^T \cdots (\mathbf{d}_t^{T-1}(l))^T]^T$ where $\mathbf{d}_t^m(l) = \text{vec}(\mathbf{a}^m_{\Lambda_t(l,1)}(\mathbf{b}^m_{\Lambda_t(l,2)})^T)$ with $\Lambda_t(l,i)$ the (l,i)th element in the index set Λ_t at the tth iteration, and $\mathbf{D}_t = [\mathbf{d}_t(1) \ldots \mathbf{d}_t(t)]$. Here, $\mathbf{a}_j^m$ denotes the jth column of the matrix $\mathbf{A}^m$ and $\mathbf{b}_j^m$ denotes the jth column of the matrix $\mathbf{B}^m$. $\bar{\mathbf{B}}$ denotes the conjugate of matrix $\mathbf{B}$. Once $\mathbf{X}$ is recovered, the delays and azimuths are estimated as

$$\hat{\tau}_l = \frac{\tau}{TN} \Lambda_L(l,1), \tag{31}$$

$$\hat{\vartheta}_l = -1 + \frac{2}{TR} \Lambda_L(l,2). \tag{32}$$

The projection performed in step 2 of the algorithm combines single channel processing with range–azimuth beamforming. The former coherently processes the second term of (23), which appears in the matrix $\mathbf{A}$, while range–azimuth beamforming over the channels coherently processes the first and third terms of (23), which are contained in $\mathbf{A}$ and $\mathbf{B}$, respectively. The FDMA narrowband assumption reconciliation is due to the additional third term of (15), contained in $\mathbf{B}$, thus enhancing range–azimuth resolution capabilities by simply updating the phase term for each channel.

The improved performance of the iterative approach over noniterative target recovery with high dynamic range is illustrated in simulations in Section V. There, we also compare our FDMA approach with classic CDMA, when using a noniterative recovery method in the former. In particular, we only use one iteration of Algorithm 1, which is equivalent to the classic approach. This demonstrates that our FDMA method outperforms CDMA due to the high range–azimuth resolution capabilities stemming from the reconciliation between the individual narrowband assumption and the large overall bandwidth.

B. Range–Azimuth-Doppler Recovery

Besides τ_l and ϑ_l lying on the grid defined in (25), we assume that the Doppler frequency f_l^D is limited to the Nyquist grid as well, defined by the CPI as

$$f_l^D = -\frac{1}{2\tau} + \frac{1}{P\tau} u_l, \tag{33}$$

where u_l is an integer satisfying $0 \le u_l \le P-1$. Let $\mathbf{Z}^m$ be the $NR \times P$ matrix with qth column given by the vertical concatenation of $y_{m,q}^p[k]$, such that the $(k+qN, p)$th element of $\mathbf{Z}^m$ is given by $(\mathbf{Z}^m)_{(k+qN,p)} = y_{m,q}^p[k - N/2]$, defined in (22), for $0 \le k \le N-1$ and $0 \le q \le R-1$. We can then write $\mathbf{Z}^m$ as

$$\mathbf{Z}^m = \left(\mathbf{B}^m \otimes \mathbf{A}^m\right) \mathbf{X}_D \mathbf{F}^T, \tag{34}$$

where the $N \times TN$ matrix $\mathbf{A}^m$ and the $R \times TR$ matrix $\mathbf{B}^m$ are defined as in Section IV-A and $\mathbf{F}$ denotes the $P \times P$ Fourier matrix up to column permutation. The matrix $\mathbf{X}_D$ is a $T^2NR \times P$ sparse matrix that contains the values α_l at the L indices $(r_l TN + s_l, u_l)$.

Our goal is now to recover $\mathbf{X}_D$ from the measurement matrices $\mathbf{Z}^m$, $0 \le m \le T-1$. The time, spatial, and frequency resolution stipulated by $\mathbf{X}_D$ are $\frac{\tau}{TN} = \frac{1}{B_{\text{tot}}}$ with $B_{\text{tot}} = TB_h$, $\frac{2}{TR}$, and $\frac{1}{P\tau}$, respectively, as in classic CDMA processing.

To jointly recover the range, azimuth, and Doppler frequency of the targets, we apply the concept of Doppler

focusing from [66] to our setting. Once the Fourier coefficients (22) are processed, we perform Doppler focusing for a specific frequency ν, that is

$$\begin{aligned}\Phi^{\nu}_{m,q}[k] &= \sum_{p=0}^{P-1} y^{p}_{m,q}[k] e^{j2\pi\nu p\tau} \\ &= \sum_{l=1}^{L} \alpha_l e^{j2\pi\beta_{mq}\vartheta_l} e^{-j\frac{2\pi}{\tau}(k+f_m\tau)\tau_l} \sum_{p=0}^{P-1} e^{j2\pi(\nu-f_l^D)p\tau},\end{aligned} \tag{35}$$

for $-\frac{N}{2} \le k \le -\frac{N}{2}-1$. Following the same argument as in [66], it holds that

$$\sum_{p=0}^{P-1} e^{j2\pi(\nu-f_l^D)p\tau} \cong \begin{cases} P & |\nu - f_l^D| < \frac{1}{2P\tau} \\ 0 & \text{Otherwise.} \end{cases} \tag{36}$$

Therefore, for each focused frequency ν, (35) reduces to a two-dimensional (2-D) problem. We note that Doppler focusing increases the SNR by a factor a P, as can be seen in (36).

Algorithm 2 solves (34) for $0 \le m \le T-1$ using Doppler focusing. Note that step 1 can be performed using the fast Fourier transform. In the algorithm description, vec($\mathbf{Z}$) is defined as in the previous section, $\mathbf{e}_t(l) = [(\mathbf{e}_t^0(l))^T \cdots (\mathbf{e}_t^{T-1}(l))^T]^T$ where $\mathbf{e}_t^m(l) = \text{vec}((\mathbf{B}^m \otimes \mathbf{A}^m)_{\Lambda_t(l,2)TN+\Lambda_t(l,1)}(\mathbf{F}^m_{\Lambda_t(l,3)})^T)$ with $\Lambda_t(l,i)$ the (l,i)th element in the index set Λ_t at the tth iteration, and $\mathbf{E}_t = [\mathbf{e}_t(1) \ldots \mathbf{e}_t(t)]$. Once $\mathbf{X}_D$ is recovered, the delays and azimuths are given by (31) and (32), respectively, and the Doppler frequencies are estimated as

$$\hat{f}_l^D = -\frac{1}{2\tau} + \frac{\Lambda_L(l,3)}{P\tau}. \tag{37}$$

Similarly to the one-pulse case, the minimal number of channels required for perfect recovery of $\mathbf{X}_D$ with L targets in noiseless settings is $TR \ge 2L$ with a minimal number of $TN \ge 2L$ samples per receiver and $P \ge 2L$ pulses per transmitter [55].

Algorithm 2: Simultaneous 3D Recovery Based OMP With Focusing.

Input: Observation matrices $\mathbf{Z}^m$, measurement matrices $\mathbf{A}^m$, $\mathbf{B}^m$, for all $0 \le m \le T-1$

Output: Index set Λ containing the locations of the non zero indices of $\mathbf{X}_D$, estimate for sparse matrix $\hat{\mathbf{X}}_D$

1: Perform Doppler focusing for $0 \le i \le N-1$, $0 \le j \le R-1$ and $0 \le \nu \le P-1$:
$$\mathbf{\Phi}^{(m,\nu)}_{i,j} = (\mathbf{Z}^m \bar{\mathbf{F}})_{i+jN,\nu}.$$
2: Initialization: residual $\mathbf{R}_0^{(m,\nu)} = \mathbf{\Phi}^{(m,\nu)}$, index set $\Lambda_0 = \emptyset$, $t = 1$
3: Project residual onto measurement matrices for $0 \le \nu \le P-1$:
$$\mathbf{\Psi}^{\nu} = \mathbf{A}^H \mathbf{R}^{\nu} \bar{\mathbf{B}},$$
where $\mathbf{A}$ and $\mathbf{B}$ are defined in (28) and (29), respectively, and $\mathbf{R}^{\nu} = \text{diag}([\mathbf{R}_{t-1}^{(0,\nu)} \cdots \mathbf{R}_{t-1}^{(T-1,\nu)}])$ is block diagonal
4: Find the three indices $\lambda_t = [\lambda_t(1)\,\lambda_t(2)\,\lambda_t(3)]$ such that
$$[\lambda_t(1) \quad \lambda_t(2) \quad \lambda_t(3)] = \underset{i,j,\nu}{\arg\max} \left|\mathbf{\Psi}^{\nu}_{i,j}\right|$$
5: Augment index set $\Lambda_t = \Lambda_t \bigcup \{\lambda_t\}$
6: Find the new signal estimate
$$\hat{\alpha} = [\hat{\alpha}_1 \ldots \hat{\alpha}_t]^T = (\mathbf{E}_t^T \mathbf{E}_t)^{-1} \mathbf{E}_t^T \text{vec}(\mathbf{Z})$$
7: Compute new residual
$$\mathbf{R}_t^{(m,\nu)} = \mathbf{R}_0^{(m,\nu)} - \sum_{l=1}^{t} \alpha_l \mathbf{a}^m_{\Lambda_t(l,1)} \left(\mathbf{b}^m_{\Lambda_t(l,2)}\right)^T \left(\mathbf{f}_{\Lambda_t(l,3)}\right)^T \mathbf{f}_{\nu}$$
8: If $t < L$, increment t and return to step 3, otherwise stop
9: Estimated support set $\hat{\Lambda} = \Lambda_L$
10: Estimated matrix $\hat{\mathbf{X}}_D$: $(\Lambda_L(l,2)TN + \Lambda_L(l,1), \Lambda_L(l,3))$-th component of $\hat{\mathbf{X}}_D$ is given by $\hat{\alpha}_l$ for $l = 1, \ldots, L$ while rest of the elements are zero

V. SIMULATIONS

In this section, we present numerical experiments illustrating our FDMA approach and compare our method with classic MIMO processing using CDMA.

A. Preliminaries

Throughout the experiments, the standard MIMO system is based on a virtual array, as depicted in Fig. 1 generated by $T = 20$ transmit antennas and $R = 20$ receive antennas, yielding an aperture $\lambda Z = 6$ m. We consider a random array configuration where the transmitters and receivers' locations are selected uniformly at random over the aperture Z for each realization. We use FDMA waveforms $h_m(t)$ such that $f_m = (i_m - \frac{T-1}{2})B_h$, where i_m are integers chosen uniformly at random in $[0, T)$, for $0 \le m \le T-1$, and all frequency bands within $[-\frac{T}{2}B_h, \frac{T}{2}B_h]$ are used for transmission. We consider the following parameters: PRI $\tau = 100\,\mu$s, bandwidth $B_h = 5$ MHz and carrier frequency $f_c = 10$ GHz. We simulate targets from the Swerling-0 model with identical amplitudes and random phases. The received signals are corrupted by uncorrelated additive Gaussian noise with power spectral density N_0. The SNR is defined as

$$\text{SNR} = \frac{\frac{1}{T_w}\int_0^{T_w} |h_0(t)|^2 \text{d}t}{N_0 B_h}, \tag{38}$$

where T_w is the pulse time.

We consider a hit-or-miss criterion according to the Rayleigh resolution as performance metric. A "hit" is defined as a range–azimuth estimate that is identical to the true target position up to one Nyquist bin (grid point) defined as $1/TB_h$ and $2/TR$ for the range and azimuth, respectively. In pulse-Doppler settings, a "hit" is proclaimed

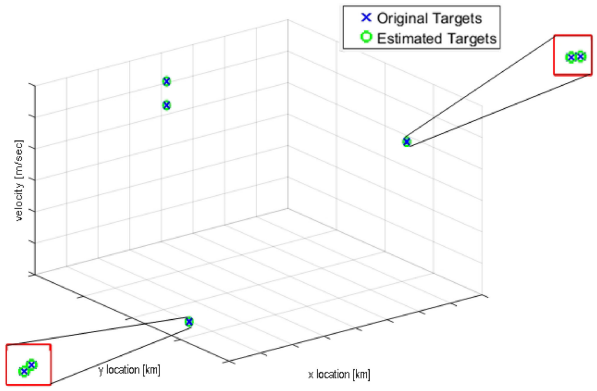

Fig. 6. Range–azimuth-Doppler recovery for $L = 6$ targets and SNR $= -10$ dB.

if the recovered Doppler is identical to the true frequency up to one Nyquist bin of size $1/P\tau$, in addition to the two previous conditions.

B. Numerical Results

We first consider a sparse target scene with $L = 6$ targets including a couple of targets with close ranges, a couple with close azimuths and another couple with close velocities. We use $P = 10$ pulses and the SNR is set to -10 dB. As can be seen in Fig. 6, all targets are perfectly recovered, demonstrating high resolution in all dimensions. Here, the range and azimuth are converted to 2-D x and y locations.

We next turn to the range–azimuth coupling issue and discuss the impact of the choice of antennas' locations and transmissions' carrier frequencies. As discussed in Section III-D, the conventional ULA array structure shown in Fig. 1 with carrier frequency selected on a grid, leads to ambiguity in the range–azimuth domain. In order to overcome the ambiguity issue, we adopt a random array configuration [51]. We found heuristically that a configuration with random antennas' locations along with random carriers on a grid provides better results than random carriers with a ULA structure. This is reasonable as we add more degrees of freedom for better sidelobe control. Fig. 7 shows a typical result of sidelobes for both configurations. The peak sidelobe level for the configuration with random antennas' locations is consistently lower.

We then compare our FDMA processing with classic MIMO processing using CDMA waveforms. Fig. 8 shows the hit rate of both techniques with respect to bandwidth B_h so that the total bandwidth B_{tot} is identical for both. The experiment was performed without noise so that the decrease in the performance in CDMA is due to the violation of the narrowband assumption (9). In our configuration, the delay $\eta_{mq}\vartheta_l$ resulting from the array geometry cannot be ignored since A6 does not hold, as the array aperture $\lambda Z = 6$m is 4 times the range resolution $1/TB_h = 1.25$m. When the received signal is modeled such as to artificially remove the delay differences between antennas, that is synthetically generated so that τ_l replaces $\tau_{l,mq}$ in (12), then the performance of both methods is identical, as expected. In Fig. 9, we observe that the targets with small azimuth angle

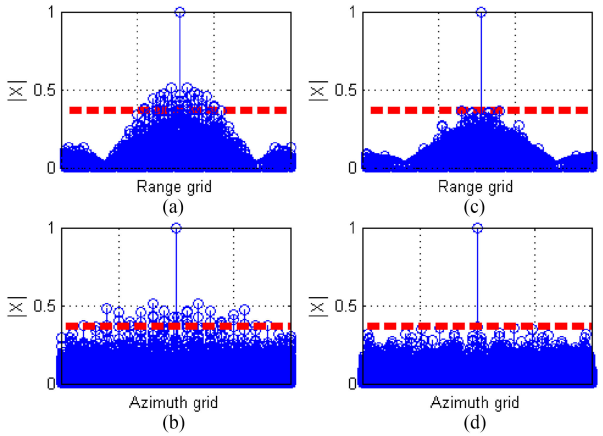

Fig. 7. Range–azimuth map in noiseless settings for random carrier frequencies along (a) range axis (b) azimuth axis, and for random antennas' locations along (c) range axis and (d) azimuth axis, for $L = 1$ target. The red dotted line indicates the peak sidelobe level for this target.

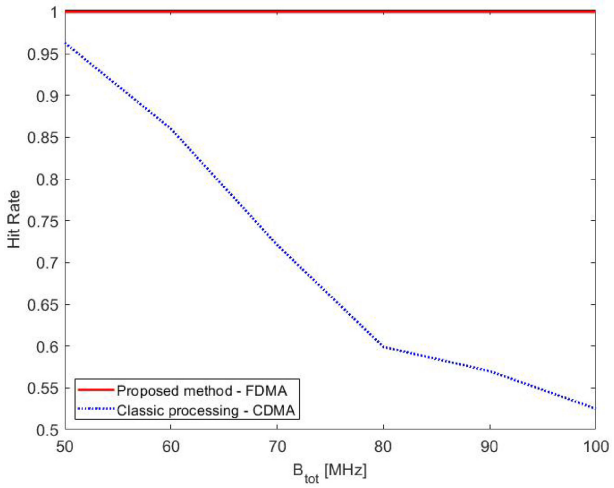

Fig. 8. Hit rate of FDMA and classic CDMA versus bandwidth.

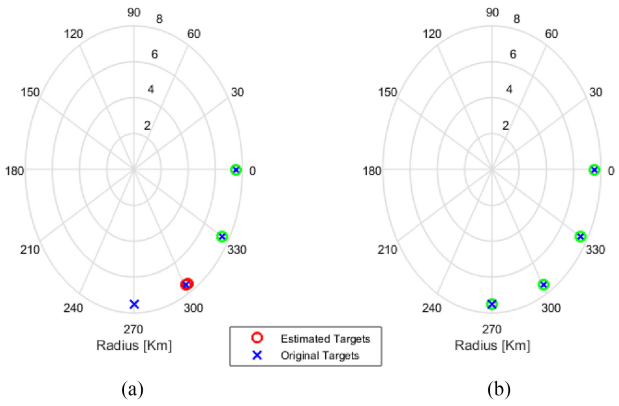

Fig. 9. Range–azimuth recovery for $L = 4$ targets using classic (a) CDMA and (b) FDMA.

θ_l are detected by both techniques, whereas targets on the end-fire direction ($\theta_l = \pm 90^\circ$, corresponds to the broadside direction) are missed by the CDMA approach. This happens because the delay differences between channels are too large, which violates the narrowband Assumption A6.

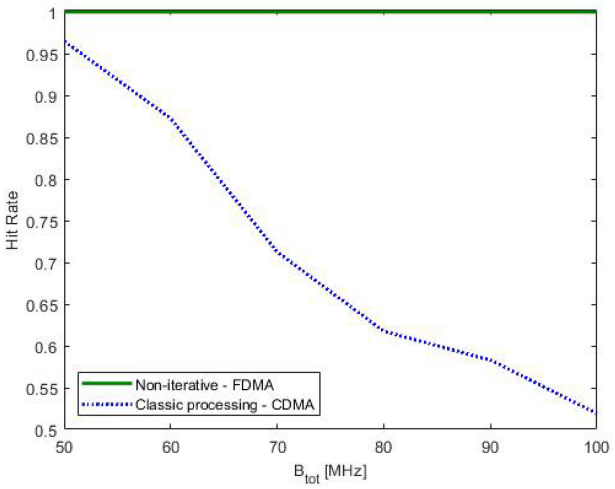

Fig. 10. Hit rate of noniterative FDMA and classic CDMA versus bandwidth.

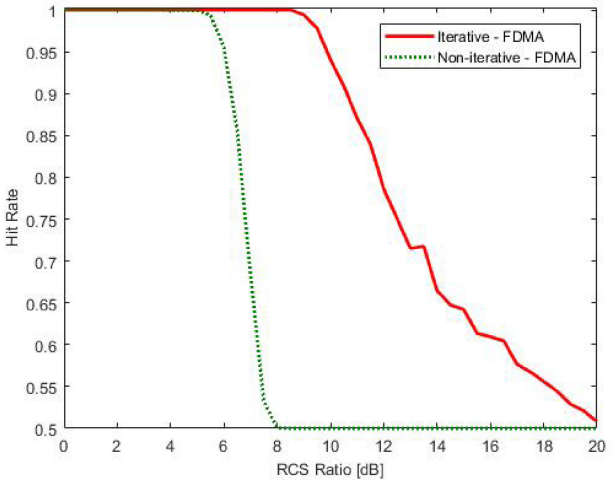

Fig. 11. Hit rate of iterative FDMA and noniterative FDMA versus RCS ratio.

In order to demonstrate that the performance gain of our FDMA approach over the classic CDMA is due to the relaxed narrowband assumption rather than our specific iterative processing, we consider a noniterative recovery approach. Fig. 10 shows our FDMA method with noniterative recovery, corresponding to one iteration of Algorithm 1. This constitutes evidence that our approach outperforms conventional CDMA processing from the relaxed narrowband assumption.

The iterative approach does boost performance of multiple targets recovery with high RCS dynamic range, allowing detection of weak targets masked by the strong ones. In doing so, we further decrease the effect of the sidelobe level and, thus, improve the detection performance. To compare both iterative and noniterative recovery, we consider $L = 2$ targets whose locations are generated uniformly at random with varying RCS ratios defined as $10\log_{10}(\frac{\alpha_{l_{\max}}}{\alpha_{l_{\min}}})$. In Fig. 11, we can see that the noniterative approach attains 50% hit rate for an RCS ratio of 8 dB, which means that the weak target is totally masked by the strong one. The iterative approach detects the weak target up to an RCS ratio of 20 dB.

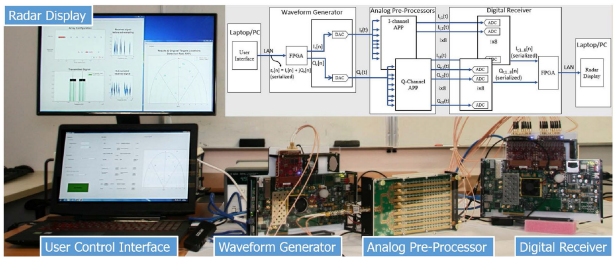

Fig. 12. FDMA MIMO prototype and user interface [68].

Each iteration of our proposed FDMA approach takes 3.9 s for 40 million range–azimuth-Doppler grid points using an Intel Core i7 PC without GPU components. We have implemented a hardware prototype realizing the FDMA MIMO processing presented here. The prototype, shown in Fig. 12, proves the hardware feasibility of our FDMA MIMO radar. Further details can be found in [67]–[69].

VI. CONCLUSION

In this article, we considered a MIMO radar configuration based on FDMA waveforms. Using FDMA allows us to relax the traditional narrowband assumption that creates a tradeoff between range and azimuth resolution. We are able to combine a large overall bandwidth for high range resolution and a large virtual array aperture for high azimuth resolution. This is enabled by the relaxed narrowband assumption that applies to the individual bandwidth of each transmitter rather than the total bandwidth as for CDMA. We thus allow widebeam beamforming while using simple phase-shifiting over the channels, providing an alternative to the classic TTD beamforming. In order to overcome one of the main FDMAs drawbacks, which limits the range resolution to the individual bandwidth, we proposed a joint processing algorithm of the channels achieving range resolution with respect to the overall bandwidth. Our system and subsequent processing copes with range–azimuth coupling, which occurs when using FDMA, by using a random array configuration along with random carrier allocation. The digital processing is a feasible iterative CS-based approach for simultaneous sparse recovery with robustness to a multiple target scenario with high dynamic range. Simulations illustrated the increased resolution obtained by our approach in comparison with classic CDMA, leading to the better detection performance.

REFERENCES

[1] E. Fishler, A. Haimovich, R. Blum, D. Chizhik, L. Cimini, and R. Valenzuela
MIMO radar: An idea whose time has come
In *Proc. IEEE Radar Conf.*, 2004, pp. 71–78.

[2] J. Li and P. Stoica
MIMO Radar Signal Processing. Hoboken, NJ, USA: Wiley, 2009.

[3] M. Lesturgie
Some relevant applications of MIMO to radar
In *Proc. IEEE Int. Radar Symp.*, 2011, pp. 714–721.

[4] A. Martinez-Vazquez and J. Fortuny-Guasch
UWB MIMO radar arrays for small area surveillance applications
In *Proc. IET Eur. Conf. Antennas Propag.*, 2007, pp. 1–6.

[5] S. Lutz, K. Baur, and T. Walter
77 GHz lens-based multistatic MIMO radar with colocated antennas for automotive applications
In *Proc. IEEE Int. Microw. Symp. Dig.*, 2012, pp. 1–3.

[6] K. Schuler, M. Younis, R. Lenz, and W. Wiesbeck
Array design for automotive digital beamforming radar system
In *Proc. IEEE Int. Radar Conf.*, 2005, pp. 435–440.

[7] J.-H. Kim, A. Ossowska, and W. Wiesbeck
Investigation of MIMO SAR for interferometry
In *Proc. IEEE Eur. Radar Conf.*, 2007, pp. 51–54.

[8] S. Anderson and W. Anderson
A MIMO technique for enhanced clutter selectivity in a multiple scattering environment: Application to HF surface wave radar
In *Proc. Int. Conf. Electromagn. Adv. Appl.*, 2010, pp. 133–136.

[9] X. P. Masbernat, M. G. Amin, F. Ahmad, and C. Ioana
An MIMO-MTI approach for through-the-wall radar imaging applications
In *Proc. IEEE Int. Waveform Diversity Des. Conf.*, 2010, pp. 188–192.

[10] E. Pancera, T. Zwick, and W. Wiesbeck
Ultra wideband radar imaging: An approach to monitor the water accumulation in the human body
In *Proc. IEEE Int. Conf. Wireless Inf. Technol. Syst.*, 2010, pp. 1–4.

[11] J. Li and P. Stoica
MIMO radar with collocated antennas
IEEE Signal Process. Mag., vol. 24, no. 5, pp. 106–114, Sep. 2007.

[12] A. M. Haimovich, R. S. Blum, and L. J. Cimini
MIMO radar with widely separated antennas
IEEE Signal Process. Mag., vol. 25, no. 1, pp. 116–129, Jan. 2008.

[13] D. Bliss and K. Forsythe
Multiple-input multiple-output (MIMO) radar and imaging: degrees of freedom and resolution
In *Proc. IEEE Asilomar Conf. Signals, Syst. Comput.*, 2003, vol. 1, pp. 54–59.

[14] D. J. Rabideau and P. Parker
Ubiquitous MIMO multifunction digital array radar
In *Proc. IEEE Asilomar Conf. Signals, Syst. Comput.*, 2003, vol. 1, pp. 1057–1064.

[15] J. Li and P. Stoica
MIMO radar diversity means superiority
In *Proc. Adaptive Sensor Array Process. Workshop*, 2006, pp. 1–6.

[16] M. Cattenoz
MIMO radar processing methods for anticipating and preventing real world imperfections
Ph.D. dissertation, Dept. Signal Image Process., Université Paris Sud-Paris XI, Orsay, France, 2015.

[17] F. Gini
Waveform Design and Diversity for Advanced Radar Systems, The Institution of Engineering and Technology, London, U.K. 2012.

[18] O. Rabaste, L. Savy, M. Cattenoz, and J.-P. Guyvarch
Signal waveforms and range/angle coupling in coherent colocated MIMO radar
In *Proc. IEEE Int. Conf. Radar*, 2013, pp. 157–162.

[19] H. Sun, F. Brigui, and M. Lesturgie
Analysis and comparison of MIMO radar waveforms
In *Proc. IEEE Int. Radar Conf.*, 2014, pp. 1–6.

[20] J. H. Ender and J. Klare
System architectures and algorithms for radar imaging by MIMO-SAR
In *Proc. IEEE Int. Radar Conf.*, 2009, pp. 1–6.

[21] J. Dorey and G. Garnier
RIAS, synthetic impulse and antenna radar
ONDE ELECTRIQUE, vol. 69, pp. 36–44, 1989.

[22] M. Pan and B. Chen
MIMO high frequency surface wave radar using sparse frequency FMCW signals
Int. J. Antennas Propag., vol. 2017, 2017, Art. no. 7514916.

[23] Y. Liu, H. Ruan, L. Wang, and A. Nehorai
The random frequency diverse array: A new antenna structure for uncoupled direction-range indication in active sensing
IEEE J. Sel. Topics Signal Process., vol. 11, no. 2, pp. 295–308, Mar. 2017.

[24] J. P. Stralka, R. M. Thompson, J. Scanlan, and A. Jones
MISO radar beamforming demonstration
In *Proc. IEEE RadarCon.*, 2011, pp. 889–894.

[25] P. Vaidyanathan and P. Pal
MIMO radar, SIMO radar, and IFIR radar: A comparison
In *Proc. Asilomar Conf. Signals, Syst. Comput.*, 2009, pp. 160–167.

[26] B. Donnet and I. Longstaff
MIMO radar, techniques and opportunities
In *Proc. IEEE Eur. Radar Conf.*, 2006, pp. 112–115.

[27] B. Donnet and I. Longstaff
Combining MIMO radar with OFDM communications
In *Proc. IEEE, Eur. Radar Conf.*, 2006, pp. 37–40.

[28] N. Levanon and E. Mozeson
Radar Signals. Hoboken, NJ, USA: Wiley, 2004.

[29] D. R. Wehner
High Resolution Radar. Norwood, MA, USA: Artech House, 1987.

[30] R. T. Lord
Aspects of stepped-frequency processing for low-frequency SAR systems
Ph.D. dissertation, Dept. Elect. Eng., University of Cape Town, Cape Town, South Africa, 2000.

[31] R. Barker
Group synchronizing of binary digital systems
In *Communication Theory*. London, U.K.: Butterworth, 1953, pp. 273–287.

[32] D. Tse and P. Viswanath
Fundamentals of Wireless Communication. Cambridge, U.K.: Cambridge Univ. Press, 2005.

[33] R. Gold
Optimal binary sequences for spread spectrum multiplexing (corresp.)
IEEE Trans. Inf. Theory, vol. IT-13, no. 4, pp. 619–621, Oct. 1967.

[34] D. B. Ward, R. A. Kennedy, and R. C. Williamson
Theory and design of broadband sensor arrays with frequency invariant far-field beam patterns
J. Acoustical Soc. Amer., vol. 97, no. 2, pp. 1023–1034, 1995.

[35] M. Cai *et al.*
Effect of wideband beam squint on codebook design in phased-array wireless systems
In *Proc. IEEE Global Commun. Conf.*, 2016, pp. 1–6.

[36] M. Longbrake
True time-delay beamsteering for radar
In *Proc. IEEE Nat. Aerosp. Electron. Conf.*, 2012, pp. 246–249.

[37] P. Vaidyanathan, P. Pal, and C.-Y. Chen
MIMO radar with broadband waveforms: Smearing filter banks and 2D virtual arrays
In *Proc. Asilomar Conf. Signals, Syst. Comput.*, 2008, pp. 188–192.

[38] G. Johansson, J. Borg, J. Johansson, M. L. Nordenvaad, and G. Wannberg
Simulation of post-adc digital beamforming for large aperture array radars
Radio Sci., vol. 45, no. 3, pp. 1–12, 2010.

[39] W. Fu and D. Jiang
Radar wideband digital beamforming based on time delay and phase compensation
Int. J. Electron., vol. 105, no. 7, pp. 1144–1158, 2018.

[40] S. Akiba, M. Oishi, J. Hirokawa, M. Ando, K. Minoguchi, and Y. Nishikawa
Photonic architecture for beam forming of RF phased array antenna
In *Proc. Opt. Fiber Commun. Conf.*, 2014, pp. W2A–51.

[41] J. Yao
Microwave photonics
J. Lightw. Technol., vol. 27, no. 3, pp. 314–335, Feb. 2009.

[42] A. Meijerink *et al.*
Novel ring resonator-based integrated photonic beamformer for broadband phased array receive antennas? Part I: Design and performance analysis
J. Lightw. Technol., vol. 28, no. 1, pp. 3–18, Jan. 2010.

[43] D. Marpaung, C. Roeloffzen, R. Heideman, A. Leinse, S. Sales, and J. Capmany
Integrated microwave photonics
Laser Photon. Rev., vol. 7, no. 4, pp. 506–538, 2013.

[44] R. A. Minasian
Ultra-wideband and adaptive photonic signal processing of microwave signals
IEEE J. Quantum Electron., vol. 52, no. 1, Jan. 2016, Art no. 0600813.

[45] R. Rotman, M. Tur, and L. Yaron
True time delay in phased arrays
Proc. IEEE, vol. 104, no. 3, pp. 504–518, Mar. 2016.

[46] P. F. Sammartino, C. J. Baker, and H. D. Griffiths
Frequency diverse MIMO techniques for radar
IEEE Trans. Aerosp. Electron. Syst., vol. 49, no. 1, pp. 201–222, Jan. 2013.

[47] P. Antonik, M. C. Wicks, H. D. Griffiths, and C. J. Baker
Frequency diverse array radars
In *Proc. IEEE Conf. Radar*, 2006, pp. 215–217.

[48] J. Dorey, Y. Blanchard, and F. Christophe
Le projet rias, UNE approche nouvelle du radar de surveillance aérienne
Onde Électrique, vol. 64, no. 4, pp. 15–20, 1984.

[49] C. Baixiao, Z. Shouhong, W. Yajun, and W. Jun
Analysis and experimental results on sparse-array synthetic impulse and aperture radar
In *Proc. IEEE, CIE Int. Conf. Radar*, 2001, pp. 76–80.

[50] Y. Lo
A mathematical theory of antenna arrays with randomly spaced elements
IEEE Trans. Antennas Propag., vol. AP-12, no. 3, pp. 257–268, May 1964.

[51] M. Rossi, A. M. Haimovich, and Y. C. Eldar
Spatial compressive sensing for MIMO radar
IEEE Trans. Signal Process., vol. 62, no. 2, pp. 419–430, Jan. 2014.

[52] Y. C. Eldar
Sampling Theory: Beyond Bandlimited Systems. Cambridge, U.K.: Cambridge Univ. Press, 2015.

[53] J. Xu, G. Liao, S. Zhu, L. Huang, and H. C. So
Joint range and angle estimation using MIMO radar with frequency diverse array
IEEE Trans. Signal Process., vol. 63, no. 13, pp. 3396–3410, Jul. 2015.

[54] W.-Q. Wang
Space-time coding MIMO-OFDM SAR for high-resolution imaging
IEEE Trans. Geosci. Remote Sens., vol. 49, no. 8, pp. 3094–3104, Aug. 2011.

[55] D. Cohen, D. Cohen, Y. C. Eldar, and A. M. Haimovich
Summer: Sub-Nyquist MIMO radar
IEEE Trans. Signal Process., vol. 66, no. 16, pp. 4315–4330, Aug. 2018.

[56] D. Cohen and Y. C. Eldar
Sub-Nyquist radar systems: Temporal, spectral, and spatial compression
IEEE Signal Process. Mag., vol. 35, no. 6, pp. 35–58, Nov. 2018.

[57] C.-Y. Chen
Signal processing algorithms for MIMO radar
Ph.D. dissertation, Dept. Elect. Eng., California Institute of Technology, Pasadena, CA, USA, 2009.

[58] E. Fishler, A. Haimovich, R. S. Blum, L. J. Cimini, D. Chizhik, and R. A. Valenzuela
Spatial diversity in radars—Models and detection performance
IEEE Trans. Signal Process., vol. 54, no. 3, pp. 823–838, Mar. 2006.

[59] M. Skolnik
Radar Handbook. New York, NY, USA: McGraw-Hill, 1970.

[60] M. A. Richards
Fundamentals of Radar Signal Processing. New York, NY, USA: McGraw-Hill, 2014.

[61] X. Chen, J. Guan, N. Liu, and Y. He
Maneuvering target detection via Radon-fractional fourier transform-based long-time coherent integration
IEEE Trans. Signal Process., vol. 62, no. 4, pp. 939–953, Feb. 2014.

[62] M. A. Richards, J. Scheer, W. A. Holm, and W. L. Melvin
Principles of Modern Radar. Princeton, NJ, USA: Citeseer, 2010.

[63] Y. C. Eldar and G. Kutyniok
Compressed Sensing: Theory and Applications. Cambridge, U.K.: Cambridge Univ. Press, 2012.

[64] J. Tsao and B. D. Steinberg
Reduction of sidelobe and speckle artifacts in microwave imaging: The CLEAN technique
IEEE Trans. Antennas Propag., vol. 36, no. 4, pp. 543–556, Apr. 1988.

[65] T. Wimalajeewa, Y. C. Eldar, and K. P.
Recovery of sparse matrices via matrix sketching
2012, *arXiv:1311.2448*.

[66] O. Bar-Ilan and Y. C. Eldar
Sub-Nyquist radar via Doppler focusing
IEEE Trans. Signal Process., vol. 62, no. 7, pp. 1796–1811, Apr. 2014.

[67] K. V. Mishra *et al.*
Cognitive sub-Nyquist hardware prototype of a collocated MIMO radar
In *Proc. IEEE, 4th Int. Workshop Compressed Sens. Theory Appl. Radar, Sonar Remote Sens.*, 2016, pp. 56–60.

[68] D. Cohen *et al.*
Sub-Nyquist MIMO radar prototype with doppler processing
In *Proc. IEEE, Radar Conf.*, 2017, pp. 1179–1184.

[69] K. V. Mishra, Y. C. Eldar, E. Shoshan, M. Namer, and M. Meltsin
A cognitive sub-Nyquist MIMO radar prototype
IEEE Trans. Aerosp. Electron. Syst., 2019.

David Cohen received the B.Sc. degree in electrical engineering from Bar Ilan University, Ramat Gan, Israel, in 2013 and the M.Sc degree in electrical engineering in 2018 from the Technion—Israel Institute of Technology, Haifa, Israel.

In 2016, he joined Rafael Advanced Defense Systems Ltd., Haifa, Israel, where he is currently a Research Associate with the Signal Processing Department. His research interests include theoretical aspects of signal processing, sampling theory, compressed sensing, and estimation theory with applications to advanced radar systems.

Deborah Cohen received the B.Sc. degree (*summa cum laude*) in electrical engineering in 2010 and the Ph.D. degree in electrical engineering (signal processing) in 2016 from the Technion—Israel Institute of Technology, Haifa, Israel, in 2010.

She is currently a Senior Research Scientist with the Machine Learning and Natural Language Processing Teams, Google Research Israel, Haifa, Israel. Her research interests include theoretical aspects of signal processing, compressed sensing, reinforcement learning, and conversational bots.

Dr. Cohen was awarded the Meyer Foundation Excellence Prize, in 2011. She was the recipient of the Sandor Szego Award and the Vivian Konigsberg Award for Excellence in Teaching from 2012 to 2016, the David and Tova Freud and Ruth Freud-Brendel Memorial Scholarship in 2014 and the Muriel and David Jacknow Award for Excellence in Teaching in 2015. Since 2014, she is an Azrieli Fellow.

Yonina C. Eldar (S'98–M'02–SM'07–F'12) received the B.Sc. degree in physics in 1995 and the B.Sc. degree in electrical engineering in 1996 both from Tel-Aviv University (TAU), Tel-Aviv, Israel, and the Ph.D. degree in electrical engineering and computer science in 2002 from the Massachusetts Institute of Technology (MIT), Cambridge, MA, USA.

She is currently a Professor with the Department of Mathematics and Computer Science, Weizmann Institute of Science, Rehovot, Israel. She was previously a Professor with the Department of Electrical Engineering, Technion—Israel Institute of Technology (Technion), where she held the Edwards Chair in Engineering. She is also a Visiting Professor with the MIT, a Visiting Scientist with the Broad Institute, and an Adjunct Professor with Duke University, and was a Visiting Professor with the Stanford University. She is the author of the book *Sampling Theory: Beyond Bandlimited Systems* (Cambridge University Press) and co-author of four other books published by Cambridge University Press. Her research interests are in the broad areas of statistical signal processing, sampling theory and compressed sensing, learning and optimization methods, and their applications to biology, medical imaging, and optics.

Dr. Eldar is a member of the Israel Academy of Sciences and Humanities (elected 2017) and a EURASIP Fellow. She was the recipient of many awards for excellence in research and teaching, including the IEEE Signal Processing Society Technical Achievement Award (2013), the IEEE/AESS Fred Nathanson Memorial Radar Award (2014), and the IEEE Kiyo Tomiyasu Award (2016). She was a Horev Fellow of the Leaders in Science and Technology program with the Technion and an Alon Fellow, the Michael Bruno Memorial Award from the Rothschild Foundation, the Weizmann Prize for Exact Sciences, the Wolf Foundation Krill Prize for Excellence in Scientific Research, the Henry Taub Prize for Excellence in Research (twice), the Hershel Rich Innovation Award (three times), the Award for Women with Distinguished Contributions, the Andre and Bella Meyer Lectureship, the Career Development Chair with the Technion, the Muriel and David Jacknow Award for Excellence in Teaching, and the Technion's Award for Excellence in Teaching (two times) and several best paper awards and best demo awards together with her research students and colleagues including the SIAM Outstanding Paper Prize, the UFFC Outstanding Paper Award, the Signal Processing Society Best Paper Award and the IET Circuits, Devices and Systems Premium Award, was selected as one of the 50 most influential women in Israel and in Asia, and is a highly cited researcher. She was a member of the Young Israel Academy of Science and Humanities and the Israel Committee for Higher Education. She is the Editor-in-Chief of Foundations and Trends in Signal Processing, a member of the IEEE Sensor Array and Multichannel Technical Committee and serves on several other IEEE committees. In the past, she was a Signal Processing Society Distinguished Lecturer, member of the IEEE SIGNAL PROCESSING THEORY AND METHODS and Bio Imaging Signal Processing technical committees, and was an Associate Editor for the IEEE TRANSACTIONS ON SIGNAL PROCESSING, the *EURASIP Journal of Signal Processing*, the *SIAM Journal on Matrix Analysis and Applications*, and the *SIAM Journal on Imaging Sciences*. She was a Co-Chair and Technical Co-Chair of several international conferences and workshops.